nature chemistry

Article

https://doi.org/10.1038/s41557-025-01942-5

Reserved charges in a long-lived NiOOH phase drive catalytic water oxidation

Received: 15 November 2024

Accepted: 12 August 2025

Published online: 15 September 2025

Check for updates

Xin Cui[1,3], Yunxuan Ding[1,3], Feiyang Zhang[1], Xing Cao[1], Yu Guo[1], Licheng Sun[1,2] & Biaobiao Zhang[1,2]

Although NiOOH has been widely studied as a water oxidation catalyst, its active structure and catalytic mechanism under operating conditions remain unclear. Isolating the true active phase is of great significance for further exploring the oxygen evolution reaction mechanisms in depth. Here we successfully isolated a long-lived active NiOOH phase with abundant Ni^{4+} and detected the presence of a stable Ni–O–O–Ni_2 phase in the bulk during the electrochemical oxygen evolution reaction. This phase spontaneously and continuously evolves oxygen in pure water at room temperature for several minutes without requiring an applied potential. Through online mass spectrometry, we demonstrate that spontaneous oxygen evolution proceeds via initial lattice oxygen coupling followed by continuous water oxidation at active sites. By studying this process, we show that the charges stored by the Ni^{4+} in NiOOH bulk can continuously migrate to the surface active sites to drive water oxidation. This offers guidance for the design of more advanced water oxidation catalysts and provides insights at the molecular level.

The electrochemical oxygen evolution reaction (OER) is crucial for water electrolysis[1]. However, this four-electron, four-proton process is recognized as the main limiting factor for hydrogen production owing to its sluggish kinetics[2,3]. In the past decades, numerous highly active OER electrocatalysts have been developed. Among these, nickel-containing catalysts, such as nickel oxides[4,5], double-layered nickel hydroxides[6–8], nickel sulfides[9,10] and nickel phosphides[11,12], have received considerable attention in the development of commercial alkaline water electrolysis anodes owing to their promising OER activity. Recent studies have revealed that nickel oxyhydroxide (NiOOH) obtained from these nickel-based materials is the active phase for oxygen evolution[13,14]. However, the structure of active NiOOH and its OER catalytic mechanism remain unclear.

NiOOH has two possible bulk phases: β-NiOOH, which forms prior to the OER, and γ-NiOOH, which facilitates O–O coupling. The structure of β-NiOOH is generally considered to be a derivative of the layered β-$Ni(OH)_2$ framework with half of the protons removed, leaving nickel in the +3 oxidation state[15]. By contrast, γ-NiOOH has previously been reported[16] to contain K^+ and a layered NiO_2 matrix with intercalated water molecules, with a chemical composition ranging from $NiO_2{\cdot}0.25H_2O$ to $K_{0.33}NiO_2{\cdot}1.33H_2O$. This suggests that γ-NiOOH contains a substantial amount of Ni^{4+}. Furthermore, Li et al.[17] proposed that the NiOOH phase can be represented as NiO_2H_x, where special peroxidic bonds appear when $x < 0.5$. Although γ-NiOOH with a high concentration of Ni^{4+} is considered the key active phase for the OER, uncertainty about its structural model poses a challenge to a comprehensive understanding of the OER catalytic mechanism.

The O–O coupling in γ-NiOOH is a critical step in the OER mechanism. In recent years, researchers have proposed three classic reaction pathways to explain this process: the adsorbate evolution mechanism (AEM)[18–20], the intramolecular oxygen coupling mechanism[21,22] and the lattice oxygen mechanism (LOM)[23–25]. Furthermore, there are reports indicating that the involvement of external light and oxidative intermediates can lead to the activation of alternative OER mechanisms[26–28]. Despite the development of in situ techniques[29–32], isotope tracing[33–35] and theoretical modelling[36–38], which have enabled the identification

[1]Center of Artificial Photosynthesis for Solar Fuels and Department of Chemistry, School of Science and Research Center for Industries of the Future, Westlake University, Hangzhou, China. [2]Division of Solar Energy Conversion and Catalysis at Westlake University, Zhejiang Baima Lake Laboratory Co., Ltd, Hangzhou, China. [3]These authors contributed equally: Xin Cui, Yunxuan Ding. e-mail: zhangbiaobiao@westlake.edu.cn

of oxygen evolution pathways based on the presence of metal oxo active intermediates such as O^{2-} (oxygen dianion), $O^{\cdot}$ (oxygen radical), O_2^{2-} (peroxide) and O_2^{-} (superoxide), these characterization methods still exhibit limitations under OER operating conditions. For instance, the temporal and spatial resolution are often inadequate to detect key signals of the truly active phase[39], the electrolyte may attenuate signal strength[40] and bubbles at high currents can interfere with the reliability of the signals[41]. Preserving and isolating the active phase through specific methods, followed by investigating its characteristics and reactions, is an effective approach to elucidating the mechanism of the OER.

In this study, we demonstrate that the active NiOOH (A-NiOOH) phase, isolated from OER operating conditions, can undergo spontaneous oxygen evolution (SOE) at room temperature and in the absence of an applied potential. By integrating experimental techniques, including online mass spectrometry and X-ray analysis, with theoretical calculations, we systematically investigated the structural evolution of the active phase and the underlying mechanism of SOE. Our findings reveal that SOE is primarily driven by the charge transfer of stored Ni^{4+} species from the γ-NiOOH bulk to surface active sites, thereby initiating water oxidation and oxygen release. SOE is ultimately halted by the deactivation of A-NiOOH through its transformation into β-NiOOH. This work elucidates the precise structure of the active NiOOH phase under OER conditions and its reaction mechanism during SOE, providing new insights into the OER catalytic process.

Results and discussion

SOE of isolated long-lived active phase

The active phase A-NiOOH was obtained by freeze-drying the NiOOH anode catalyst under conditions used for electrolytic water splitting (Supplementary Fig. 1). Upon introduction of A-NiOOH into pure water at room temperature, a notable number of bubbles rapidly formed on the catalyst surface and persisted for several minutes (Supplementary Video 1). This observation suggests the occurrence of an as-yet-unidentified non-electrochemical gas evolution reaction. The presence of oxygen in these bubbles was further analysed using a Clark oxygen electrode, confirming that 4 mg of A-NiOOH generated 175 nmol ml^{-1} of oxygen within 300 s (Fig. 1a). By contrast, deactivated NiOOH (A-NiOOH after oxygen evolution, denoted as D-NiOOH) was found to be incapable of releasing oxygen in water. The amount of released oxygen is positively proportional to the mass of the added A-NiOOH (Fig. 1b). Without adding water, no O_2 was detected by optical oxygen sensing (Supplementary Fig. 2), indicating that the reaction with water is necessary for the O_2 release, and the released O_2 is not from the O_2 physically adsorbed on the surface. Moreover, the dried reactive A-NiOOH can be stored in the air for several days and in a protected atmosphere (N_2) or in vacuum conditions for months. In contrast to previous works, where NiOOH undergoes chemical oxygen evolution upon direct heating in alkali or generates oxygen during electroreduction[42–45], the SOE process of A-NiOOH does not require any external energy. Therefore, these results confirm that A-NiOOH, as an active intermediate in operational OER, can produce oxygen in pure water without the need for any additional driving force.

To reveal the mechanism of SOE from A-NiOOH, it is important to track the source of the released oxygen. The use of online mass spectrometry (OLMS) for tracing the oxygen isotopes released from unlabelled A-NiOOH (denoted as [^{16}O]A-NiOOH) in $H_2{}^{18}O$ revealed two types of oxygen: $^{16}O_2$ and $^{18}O_2$ (Fig. 1c). The $^{16}O^{18}O$ signal was negligible. Moreover, it is clear that $^{16}O_2$ was initially generated at a high evolution rate within the first 100 s. After 5 s (Fig. 1c, inset), $^{18}O_2$ evolution started with an increased rate for 400 s, then was maintained at a high evolution rate for another 600 s. By contrast, $^{16}O_2$ evolution was gradually decreased after 120 s. The generation of $^{16}O_2$ can only originate from the formation of the O–O bond between the lattice oxygen ($^{16}O_{lattice}$) of the [^{16}O]A-NiOOH. The absence of $^{16}O^{18}O$ production suggests that lattice oxygen (Ni–$^{16}O_{lattice}$) cannot directly couple with adsorbed water ($H_2{}^{18}O$). The generation of $^{18}O_2$ means that the A-NiOOH can directly recombine and oxidize $H_2{}^{18}O$ into oxygen. It is noteworthy that the AEM is considered the primary OER mechanism under operating conditions[36], but the direct coupling of lattice O–O into O_2 in the SOE mechanism confirms the complexity of operating OER mechanisms.

To further verify the role of lattice O–O coupling in the SOE process of A-NiOOH, tetramethylammonium cation (TMA^+) molecular probes were used to capture the $*O_2^{2-}$ intermediates generated during this process[46,47]. Figure 1d illustrates that, upon testing the oxygen released by A-NiOOH at the oxygen electrode, the addition of TMA^+ decelerated the O_2 release and diminished the total amount of oxygen produced. This observation suggests that lattice O–O coupling occurs during the SOE process, leading to the formation of $*O_2^{2-}$ intermediates.

Based on the results of the isotope and TMA^+ probe experiments, an oxygen evolution pathway can be proposed for SOE (Fig. 2). A-NiOOH is an active intermediate state that is instantaneously separated and retained during the electrochemical OER process, it therefore is full of reserved charge like a battery[48]. The reserved charge first can drive the ^{16}O–^{16}O coupling of the stored lattice oxygen, thereby releasing $^{16}O_2$ in water. Following the release of a $^{16}O_2$ molecule, the catalytic site is replenished by new $H_2{}^{18}O$ molecules, and the reserved internal charge migrates to active sites on the surface to complete the oxidation of the recombined $H_2{}^{18}O$ to $^{18}O_2$. According to this mechanism, oxygen will be continuously generated from water oxidation until all internal charges are depleted, and all high-valence nickel is converted to low-valence nickel.

Structural changes of A-NiOOH during SOE

The oxygen evolution pathway for SOE is clear, as shown in Fig. 2. However, the revelation of the detailed reaction mechanism of SOE requires characterization of the structural changes of A-NiOOH before and after SOE. First, scanning electron microscopy (SEM) observations revealed that both A-NiOOH (Supplementary Fig. 3) and D-NiOOH (Supplementary Fig. 4) are composed of nanosheets assembled into microcolumnar structures, indicating that the morphology of the active phase remains largely unchanged during the SOE process. This suggests a high degree of structural stability. To further investigate the changes in the active phase, powder X-ray diffraction (XRD) and aberration-corrected high-angle annular dark-field scanning transmission electron microscopy (AC-HAADF-STEM) were used to characterize the A-NiOOH and D-NiOOH. XRD analysis confirms that the structure of A-NiOOH is primarily formed by the γ-NiOOH phase (PDF card number 06-0075, Fig. 3a). The exposed (101) facet of A-NiOOH was observed using AC-HAADF-STEM, as shown in Supplementary Fig. 3. The measured interplanar spacing of 0.241 nm corresponds to the (101) plane of γ-NiOOH. XRD (Fig. 3a) shows the presence of a distinct β-NiOOH phase (PDF card number 06-0141) in D-NiOOH, with the disappearance of the γ-NiOOH phase, and the (105) planes of β-NiOOH were also observed in the AC-HAADF-STEM (Supplementary Fig. 4). Notably, A-NiOOH was rinsed with water during the isolation process, which may have led to a transitory occurrence of SOE, forming a small amount of β-NiOOH (Fig. 3a), explaining the mixed phase in A-NiOOH.

To confirm the structure of the A-NiOOH and D-NiOOH, quantitative analysis of the metal valence states was further conducted using X-ray absorption spectroscopy (XAS) and atomic-resolution electron energy loss spectroscopy (EELS). The X-ray absorption near-edge structure (XANES) spectrum of A-NiOOH exhibits an intermediate valence state between $H_4I_2K_2NiO_{12}$ (Ni^{4+}) and $LiNiO_2$ (Ni^{3+}) (Fig. 3b). To determine the oxidation state of nickel, the photon energies at the XANES half-height of four standard valence nickel compounds (0, +2, +3 and +4) were analysed (Fig. 3b, inset). The results indicated that the average valence state of the nickel in A-NiOOH was +3.64, which is consistent with the typical average nickel valence state in γ-NiOOH. The XANES spectrum of D-NiOOH is similar to that of $LiNiO_2$ (Fig. 3b),

https://doi.org/10.1038/s41557-025-01942-5

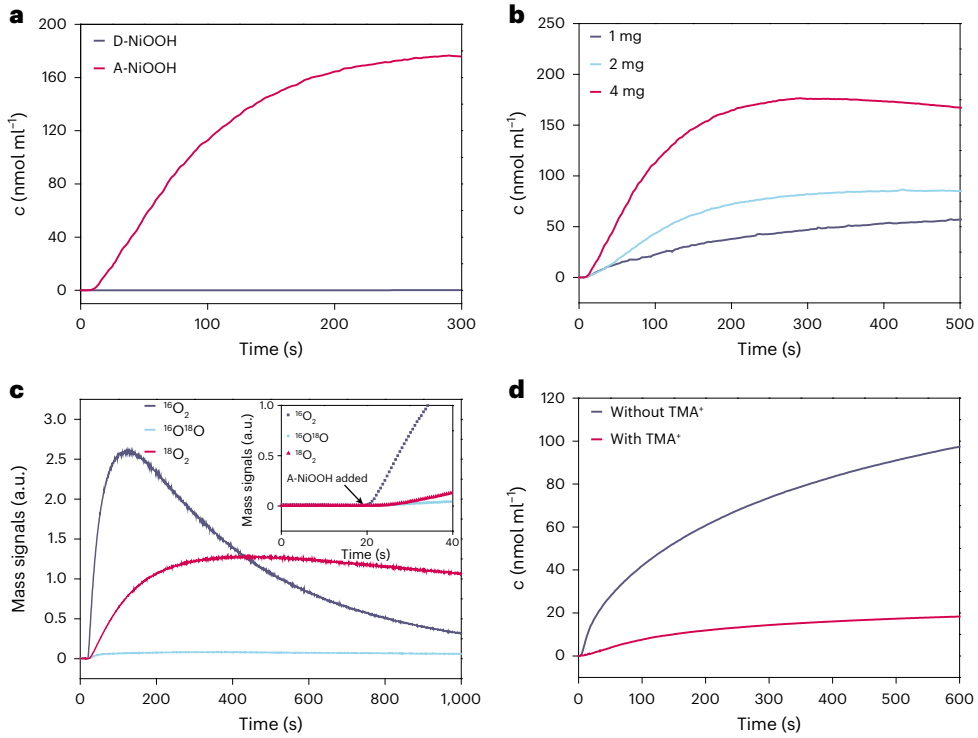

Fig. 1 | Identification of the O_2 release path and the O–O coupling process. **a**, The calibrated Clark oxygen electrode exhibits a typical oxygen response in pure water for A-NiOOH and D-NiOOH with the same mass. **b**, The oxygen signal response of different masses of A-NiOOH in pure water. **c**, OLMS shows $^{16}O^{16}O$ ($m/z = 32$), $^{16}O^{18}O$ ($m/z = 34$) and $^{18}O^{18}O$ ($m/z = 36$) signals from A-NiOOH-released oxygen in $H_2{}^{18}O$. Inset: changes in the oxygen signal during the first 40 s of the OLMS experiment; the arrow indicates the time at which A-NiOOH was added to $H_2{}^{18}O$. **d**, The oxygen signal response of A-NiOOH in pure water with or without TMA$^+$. a.u., arbitrary units.

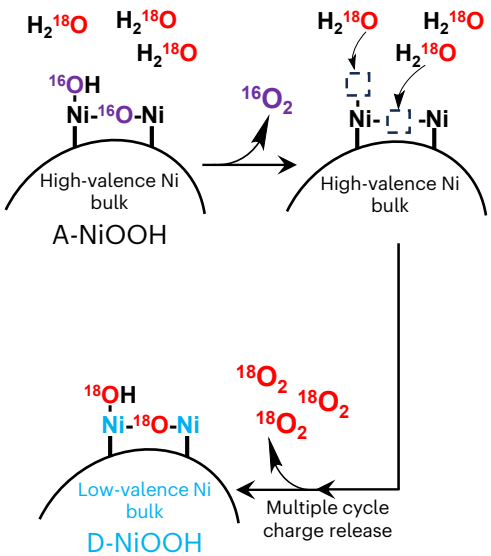

Fig. 2 | SOE pathway. Illustration of water oxidation driven by reserved charge.

supported by the calculated average valence state of +2.93 for nickel in D-NiOOH (Fig. 3b, inset). In the EELS spectra, the peak position of the nickel L_2/L_3 edge shows a pronounced low-energy shift (Fig. 3c and Supplementary Fig. 5), indicating the reduction of a large amount of Ni^{4+}, which is consistent with the XAS results shown in Fig. 3b. The related structural changes are also demonstrated by the extended X-ray absorption fine structure (EXAFS) spectra (Supplementary Fig. 6) and the X-ray pair distribution function (PDF) analysis (Fig. 3d). The R-space EXAFS spectra shows that the lengths of the Ni–O and Ni–Ni bonds were increased, confirming the decrease of the nickel valence state. The bonding information derived from the PDF data gives bond lengths of 1.903 Å and 2.864 Å for Ni–O and Ni–Ni in A-NiOOH, respectively, which were increased to 1.968 Å and 2.907 Å in D-NiOOH, respectively. Thus, the Ni^{4+} (γ-NiOOH) in A-NiOOH was transferred to the Ni^{3+} (β-NiOOH) in D-NiOOH through SOE, whereby a large number of Ni^{4+} species are proposed as the energy source driving SOE.

Furthermore, Raman spectroscopy was carried out to identify the fine structure of A-NiOOH and D-NiOOH, such as the active oxygen species[49–52]. The Raman spectrum of A-NiOOH exhibits sharp features at 475 and 553 cm^{-1}, corresponding to the E_g bending vibration (δ(Ni–O)) and the A_{1g} stretching vibration (ν(Ni–O)) mode (Fig. 4a). The broad feature between 850 and 1,200 cm^{-1} can be assigned to the O–O stretch of the active oxygen species (Fig. 4b). To further reveal this special O–O structure, isotopic labelling experiments were carried out. The utilization of ^{18}O isotopic labelling for A-NiOOH led to a redshift of 25 cm^{-1} in the Ni–O vibrational mode (Fig. 4c and Supplementary Fig. 7a). Moreover, the O–O stretching mode was redshifted about 50 cm^{-1} (Supplementary Fig. 7b), confirming that the broad feature between 850 and 1,200 cm^{-1} involves a species containing two oxygen atoms bonded directly, such as Ni–O–O–Ni or Ni–O–O–H. To further identify the oxygen release site and the O–O structure, electrochemical activation of A-NiOOH was performed under identical conditions using both H_2O and D_2O. The vibrational frequency of the O–O species remains unchanged in the presence of D_2O (Supplementary Fig. 8). This indicates that no hydrogen interacts with the observed O–O species, suggesting that the O–O bond is more accurately characterized as a Ni–O–O–Ni species. Interestingly, the broad peak in the range 850–1,200 cm^{-1} was also observed in the Raman spectrum of D-NiOOH (Fig. 4b), suggesting that the Ni–O–O–Ni moiety is a stable structure

https://doi.org/10.1038/s41557-025-01942-5

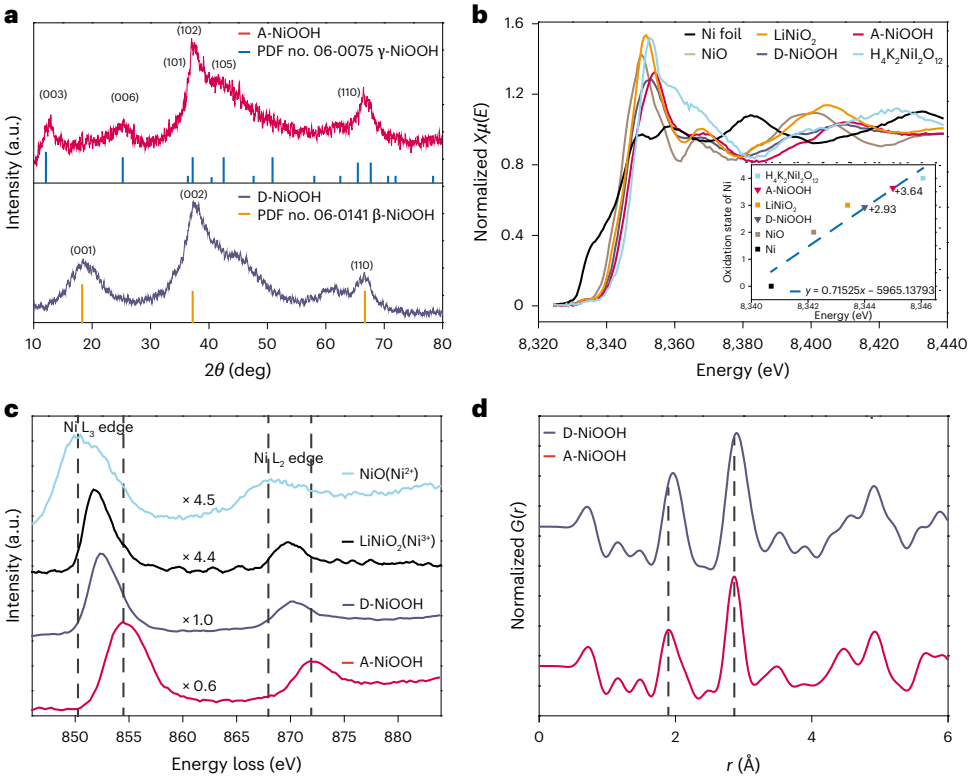

Fig. 3 | Structure changes of A-NiOOH before and after SOE. a, XRD patterns. **b**, XANES spectra at the nickel K-edge of A-NiOOH and D-NiOOH, nickel foil, NiO, $LiNiO_2$ and $H_4I_2K_2NiO_{12}$. Inset: oxidation state of various nickel compounds obtained from nickel K-edge XANES. **c**, EELS spectra of the nickel L-edge for A-NiOOH, D-NiOOH, NiO and $LiNiO_2$. The left and right dashed lines indicating the Ni L_3 and L_2 edge energy losses mark the minimum and maximum energy loss values, respectively, of the corresponding peaks for the four samples. **d**, The reduced pair PDF for A-NiOOH and D-NiOOH. The positions of the bond lengths on the *x* axis corresponding to the two dashed lines represent the peaks of A-NiOOH at 1.903 Å and 2.864 Å, respectively.

that did not directly engage in the reaction of O_2 formation. Three possible Ni–O–O–Ni structures present in A-NiOOH are illustrated in Supplementary Fig. 9. Density functional theory (DFT) calculations found that the Ni–O–O–Ni structure on the surface cannot exist stably; by contrast, the internal Ni–O–O–Ni structure is able to exist stably, which is consistent with the literature[17,53]. This unique structure coordinating with three nickel ions is referred to as Ni–O–O–Ni_2. Finally, a structure model with abundant Ni^{4+} and a stable Ni–O–O–Ni_2 moiety is proposed for A-NiOOH in Supplementary Fig. 10.

To further determine the O–O coupling process of A-NiOOH during the SOE process, the elemental ratio during the transformation from A-NiOOH to D-NiOOH was investigated using energy-dispersive X-ray spectroscopy (EDS). The results indicate that the Ni:O atomic ratio changed from 1:1.98 to 1:1.67 (Supplementary Figs. 11 and 12), signifying a reduction in oxygen content due to the release of lattice oxygen from A-NiOOH during the SOE process. X-ray photoelectron spectroscopy (XPS) analysis of A-NiOOH before and after SOE confirmed the involvement of lattice oxygen in the formation of O_2. Following oxygen evolution, the oxygen 1*s* signal at 529.3 eV noticeably decreased, while the adsorbed H_2O signal at 533.2 eV markedly increased (Fig. 4d). This suggests that lattice oxygen participated in the evolution of O_2, and the resulting oxygen vacancies were occupied by H_2O. The changes in the chemical environment of these active phases are consistent with the SOE process, as illustrated in Fig. 2.

The above results identify the reaction process of A-NiOOH, which includes the oxidation of water to release oxygen and the subsequent transformation into D-NiOOH under charge-driven conditions (Fig. 5a). The SOE process of A-NiOOH is driven by charge transfer from the internal Ni^{4+} to the surface active sites, leading to the coupling of lattice oxygen to form O_2. This is followed by the continuous oxidation of H_2O to O_2 at the same active site until the internal charge of the active phase is depleted, ultimately resulting in the transformation into D-NiOOH (Ni^{3+}). In conjunction with the analysis of structural changes in the active phase, DFT calculations provide a detailed modelling of the structure of A-NiOOH and D-NiOOH (Fig. 5b,c).

DFT calculations of the SOE mechanism

With the structure model of A-NiOOH and D-NiOOH in hand, DFT calculations were performed to rigorously investigate the electrocatalysis and SOE processes. To theoretically confirm the isolated structure of the active intermediate from Supplementary Fig. 1, the electrocatalytic OER mechanism was initially explored (Supplementary Figs. 13 and 14). By considering the key adsorbed intermediates, namely OH*, O* and OOH*, the AEM and LOM were both taken into account. The potential-limiting step for the AEM is identified as the dehydrogenation of Ni^{4+}–OH (adsorbed OH*) with an overpotential of 0.85 V, while for the LOM, it is the dehydrogenation of Ni^{4+}–OH–Ni^{3+} (lattice OH*) with an overpotential of 0.95 V. Notably, the AEM exhibits a lower overpotential of 0.85 V compared with 0.95 V of the LOM, suggesting that the dehydrogenation of adsorbed OH* serves as the overall potential-limiting step in electrocatalysis process. Therefore, the OH*-covered configuration (S_1 in Supplementary Fig. 13) is the active structure preserved after the electrolysis process is stopped.

To investigate the dehydrogenation step in the SOE process, A-NiOOH without oxygen isotope labelling was tested for OLMS in an ^{18}O-labelled acid solution (Supplementary Fig. 15). Compared with the pure water (Fig. 1c), the rate of $^{16}O_2$ release was inhibited whereas that of $^{18}O_2$ release was enhanced, revealing two distinct dehydrogenation pathways for their formation. Further exploration of the SOE mechanism in $H_2{}^{18}O$ (Fig. 6a) demonstrated that the dehydrogenation of ^{16}OH*

https://doi.org/10.1038/s41557-025-01942-5

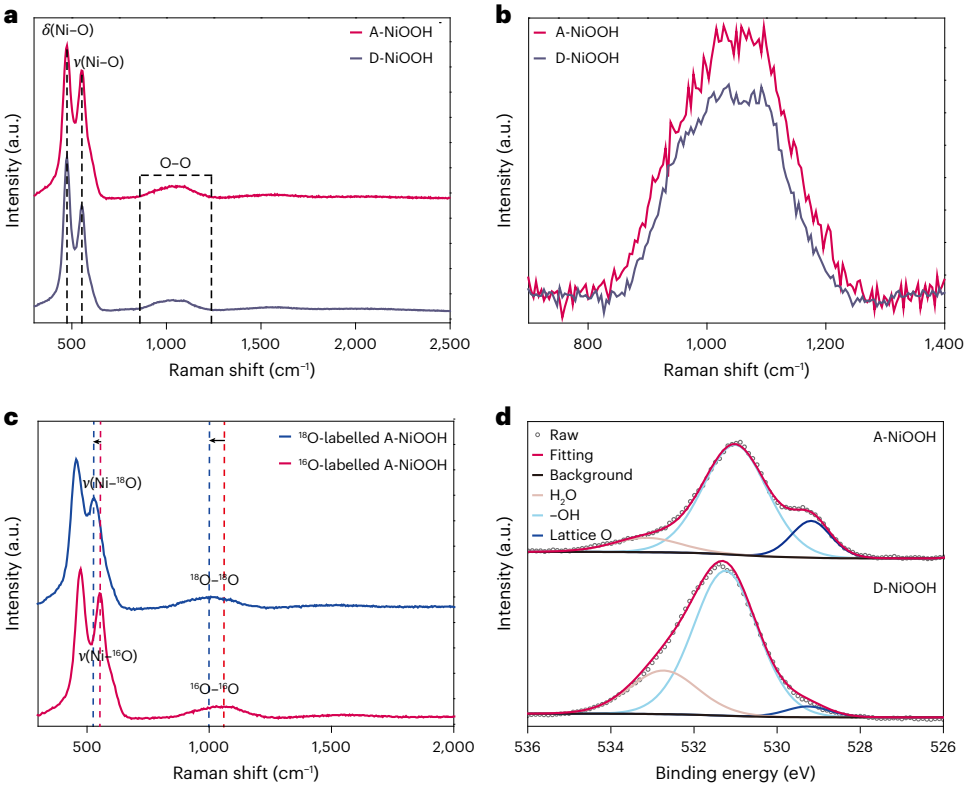

Fig. 4 | Structural characterization of A-NiOOH and D-NiOOH. a, Raman spectroscopy of A-NiOOH and D-NiOOH. **b**, Broad bands corresponding to O–O vibrations at higher frequencies. **c**, Raman spectroscopic analysis with/without ^{18}O-labelled A-NiOOH. **d**, XPS spectra of the oxygen 1*s* orbital of A-NiOOH and D-NiOOH.

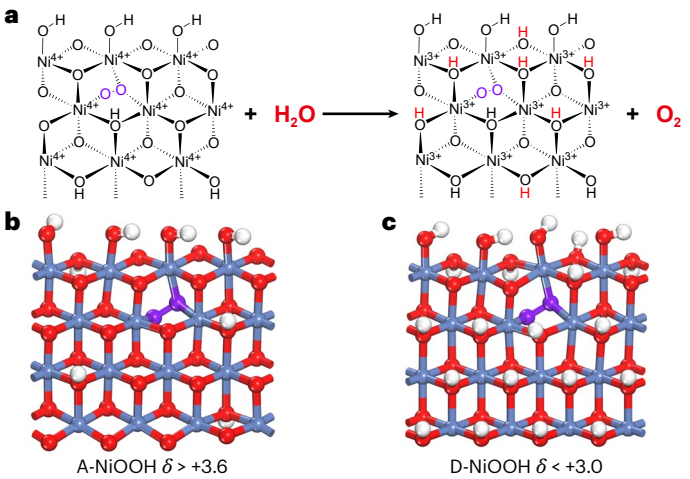

Fig. 5 | Reaction and structure models of A-NiOOH and D-NiOOH. a, The reaction equation for the reaction of A-NiOOH with water to form D-NiOOH and oxygen is as follows: A-NiOOH + H_2O → D-NiOOH + O_2. **b**,**c**, Side views of A-NiOOH (**b**) and D-NiOOH (**c**) with covered OH*. Blue, red, white and purple balls represent nickel, oxygen, hydrogen and O–O bridge, respectively.

was suppressed by high H^+ concentration. Specifically, the dehydrogenation of the adsorbed ^{16}OH* proceeds through a barrierless process of releasing a proton to form H_3O^+ with an electron reducing the sublayer Ni^{4+} to Ni^{3+} (Supplementary Fig. 16). Following the dehydrogenation step, the adsorbed ^{16}O* radical reacts with the $^{16}O_{lattice}$, forming an O–O bond. This process is spontaneous and will occur without external force due to a negative reaction free energy of −1.16 eV, which is a barrierless step as well (Supplementary Fig. 17). Additionally, this process happens along with a Ni^{4+} in the top layer being reduced to Ni^{3+}. The concerted adsorption–desorption step of $^{16}O_2$ release and $H_2{}^{18}O$ insertion occur simultaneously with a reaction free energy of −1.44 eV. The process is exothermic and can occur spontaneously. Meanwhile, owing to the oxidation of adsorbed $*O_2{}^{2-}$, the release of O_2 results in a further reduction of the nearby nickel ions to Ni^{2+} and Ni^{3+}, respectively.

The lower valence state of the nickel ion hampers water oxidation. However, the distinctive structure of A-NiOOH results in an abundance of Ni^{4+} in the bulk of the catalyst, acting as a reservoir for the high oxidation state and accepting extra electrons. Figure 6b and Supplementary Fig. 18 illustrate the electron- and hydrogen-transfer process. Following $^{16}O_2$ release, $H_2{}^{18}O$ is introduced to the oxygen vacancy site. Together with an electron, a proton from $H_2{}^{18}O$ is transferred to the lattice oxygen in the sublayer, and the charge inversely migrates to the surface-active sites. This process has an activation barrier of 1.18 eV with a reaction free energy of −0.35 eV. Then, this H* can be further transferred to the lattice oxygen in the third layer with an activation barrier of 1.50 eV. It should be noted that the presence of the O–O bridge structure within the bulk helps to transfer the H* and facilitates easier oxidation of the nickel ion, as evidenced by the lower activation barrier in the first hydrogen-transfer step compared with the second hydrogen-transfer step (the role of Ni–O–O–Ni_2 is detailed in Methods). This continuous proton-transfer process also represents a simplified phase-transformation mechanism of γ-NiOOH to β-NiOOH. Once the hydrogen transfer has caused surface nickel sites to be oxidized into the high valence state, these sites possess the necessary chemical driving force for the subsequent water oxidation.

To explore the mechanism of $^{18}O_2$ release, we consider a reaction intermediate containing a nickel ion in a high oxidation state. Following the continuous proton-transfer process, the ^{18}O from the inserted $H_2{}^{18}O$ is preserved and forms a Ni^{3+}–$^{18}O_{lattice}$–Ni^{4+} structure. Subsequently, another $H_2{}^{18}O$ from the solvent can be adsorbed on the active Ni^{3+} site, accompanied by a charge rearrangement leading to a Ni^{4+} in the top layer and a Ni^{3+} in the sublayer. This spontaneous step is exothermic

https://doi.org/10.1038/s41557-025-01942-5

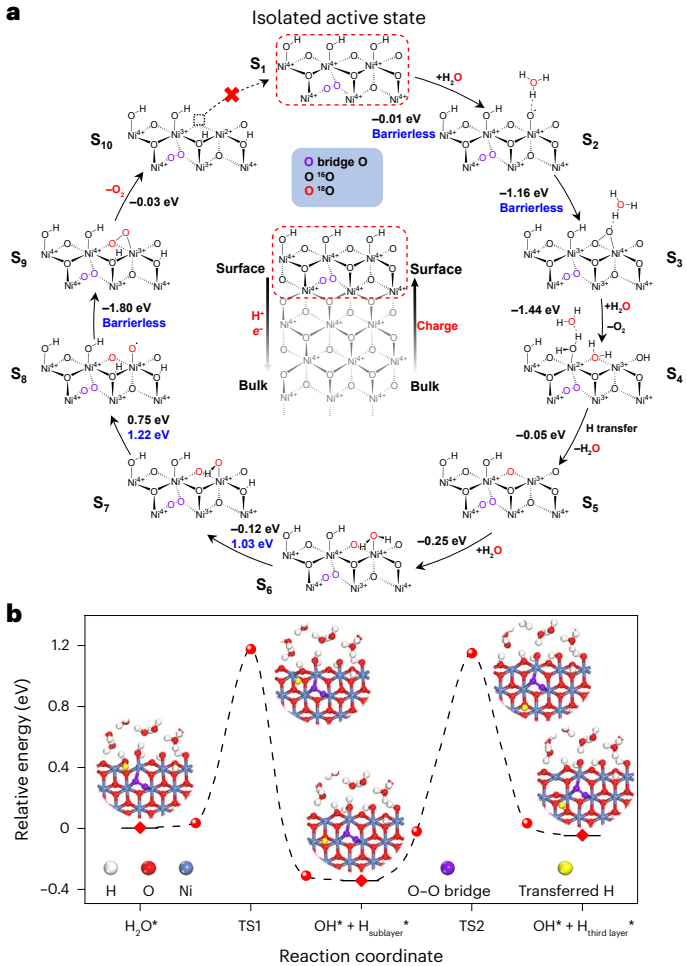

Fig. 6 | Proposed SOE mechanism and hydrogen-transfer process. a, Catalytic pathway of SOE processes. Energies marked in black and blue represent reaction free energies and activation barriers, respectively. Insert: the isolated active phase and the charge release process. **b**, Reaction free energy diagram of continuous proton-transfer process. Inserts: reaction intermediates.

with a reaction free energy of −0.25 eV. Subsequently, experimental observations suggest that the $^{18}O_2$ release rate is enhanced at low pH, differing from that of $^{16}O_2$ (Supplementary Fig. 15), indicating that the dehydrogenation of $H_2{}^{18}O$ is likely to produce adsorbed H* rather than H_3O^+. Therefore, the first dehydrogenation of $H_2{}^{18}O$* leads to an adsorbed ^{18}OH* on the nickel site and an adsorbed H* on the sublayer lattice oxygen. This process exhibits a reaction free energy of −0.12 eV and an activation barrier of 1.03 eV (Supplementary Fig. 19). The second dehydrogenation of ^{18}OH* produces an ^{18}O* radical adsorbed on the nickel site and the H* adsorbed on another sublayer lattice oxygen; this process has a free energy of 0.75 eV and an activation barrier of 1.22 eV (Supplementary Fig. 20). Hence, this step is the rate-determining step for the $^{18}O_2$ release process. O–O coupling takes place between the adsorbed ^{18}O* radical and the $^{18}O_{lattice}$, which is a barrierless process with a reaction free energy of −1.80 eV (Supplementary Fig. 21). This highlights that once the O* radical is formed, spontaneous formation of the O–O bond can occur. Finally, $^{18}O_2$ is released with a reaction free energy of −0.03 eV. Concurrently, the nickel ions on the reaction sites are reduced to Ni^{2+} and Ni^{3+}, respectively. It should be noted that the low oxidation state of the nickel ion loses its ability to oxidize water unless the H* on the sublayer lattice oxygens transfer to the bulk, leading to the reoxidation of surface nickel ions to higher valence states. The oxidation of water and the reduction of nickel ions eventually result in the phase transformation from γ-NiOOH to β-NiOOH. Once the D-NiOOH is formed with the depleted Ni^{4+} (Fig. 5c), the water oxidation reaction will stop.

SOE in the electrocatalytic OER cycle

Experimental and theoretical studies have revealed the SOE mechanism of A-NiOOH. However, another important consideration is whether the SOE process is involved in the electrocatalytic OER cycle on A-NiOOH. The first evidence supporting this proposal comes from an experiment involving the addition of TMA^+ to the H_2O. In the presence of TMA^+, the electrocatalytic OER activity of A-NiOOH markedly decreased (Supplementary Fig. 22), suggesting that O_2 release via $*O_2^{2-}$ is inhibited. This indicates that the SOE process, involving lattice O–O coupling, occurs during the electrocatalytic OER on A-NiOOH. The cyclic voltammetry curves in Supplementary Fig. 23 further confirm this finding. At the same potential, the current density during the reverse scan is higher than that during the forward scan. For example, the current density at an overpotential of 220 mV on the reverse scan curve is more than 600 mA cm^{-2} higher than during the forward scan. This portion of the current is attributed to SOE. Specifically, this phenomenon occurs owing to a substantial accumulation of A-NiOOH during the forward scan. With the accumulation of A-NiOOH, in addition to electrochemical water oxidation, SOE of A-NiOOH begins to occur during the reverse scan, adding one more oxygen evolution pathway, thereby increasing the current density. Consequently, SOE is a crucial pathway for accelerating the electrocatalytic OER process on A-NiOOH. Notably, SOE maintains considerable activity during the electrochemical process even after 40 cycles of cyclic voltammetry and prolonged electrolysis (Supplementary Figs. 24 and 25). After long-term testing, the active phase isolated remained predominantly γ-NiOOH (Supplementary Fig. 26), and continues to exhibit the capability to generate O_2 (Supplementary Fig. 27). In designing nickel-based OER catalysts, it is essential to consider the formation of more A-NiOOH phase during the electrochemical OER process.

Conclusions

We have revealed the structure and SOE process of the active phase of the NiOOH water oxidation catalyst through a rapid freeze-drying isolation method. By investigating the structural changes of A-NiOOH before and after SOE, it was found that A-NiOOH transforms from the γ-NiOOH phase (average oxidation state, +3.64) to the inactive phase β-NiOOH (average oxidation state, +2.93), while always retaining a stable peroxo compound (Ni–O–O–Ni_2) that does not participate in oxygen evolution. The SOE process of A-NiOOH involves the spontaneous transformation of γ-NiOOH to β-NiOOH accompanied by oxygen evolution. We demonstrate that the charges stored in the Ni^{4+} within the NiOOH bulk can continuously migrate to the surface active sites to drive water oxidation. Additionally, DFT calculations reasonably explained the formation of O–O bonds and the hydrogen-transfer pathway during the SOE process. This work not only elucidates the hidden SOE mechanism in operational OER using the method of isolating active phases but also provides theoretical support for the design of anode materials in water electrolysis.

Online content

Any methods, additional references, Nature Portfolio reporting summaries, source data, extended data, supplementary information, acknowledgements, peer review information; details of author contributions and competing interests; and statements of data and code availability are available at https://doi.org/10.1038/s41557-025-01942-5.

References

1. Jiao, Y., Zheng, Y., Jaroniec, M. & Qiao, S.-Z. Design of electrocatalysts for oxygen- and hydrogen-involving energy conversion reactions. *Chem. Soc. Rev.* **44**, 2060–2086 (2015).
2. Ram, R. et al. Water-hydroxide trapping in cobalt tungstate for proton exchange membrane water electrolysis. *Science* **384**, 1373–1380 (2024).

3. Duan, Y. et al. Anodic oxidation enabled cation leaching for promoting surface reconstruction in water oxidation. *Angew. Chem. Int. Ed.* **60**, 7418–7425 (2021).
4. Radinger, H. et al. Importance of nickel oxide lattice defects for efficient oxygen evolution reaction. *Chem. Mater.* **33**, 8259–8266 (2021).
5. Kuai, C. et al. Creating compressive stress at the NiOOH/NiO interface for water oxidation. *J. Mater. Chem. A* **8**, 10747–10754 (2020).
6. Wang, Y.-H. et al. Defect engineering promotes synergy between adsorbate evolution and single lattice oxygen mechanisms of OER in transition metal-based (oxy)hydroxide. *Adv. Sci.* **10**, 2303321 (2023).
7. Tao, S., Wen, Q., Jaegermann, W. & Kaiser, B. Formation of highly active NiO(OH) thin films from electrochemically deposited $Ni(OH)_2$ by a simple thermal treatment at a moderate temperature: a combined electrochemical and surface science investigation. *ACS Catal.* **12**, 1508–1519 (2022).
8. Gao, M. et al. Efficient water oxidation using nanostructured α-nickel-hydroxide as an electrocatalyst. *J. Am. Chem. Soc.* **136**, 7077–7084 (2014).
9. You, B. & Sun, Y. Hierarchically porous nickel sulfide multifunctional superstructures. *Adv. Energy Mater.* **6**, 1502333 (2016).
10. Zahran, Z. N. et al. Electrocatalytic water splitting with unprecedentedly low overpotentials by nickel sulfide nanowires stuffed into carbon nitride scabbards. *Energy Environ. Sci.* **14**, 5358–5365 (2021).
11. Xue, S., Chen, L., Liu, Z., Cheng, H.-M. & Ren, W. $NiPS_3$ nanosheet–graphene composites as highly efficient electrocatalysts for oxygen evolution reaction. *ACS Nano* **12**, 5297–5305 (2018).
12. Zeng, L. et al. Three-dimensional-networked Ni_2P/Ni_3S_2 heteronanoflake arrays for highly enhanced electrochemical overall-water-splitting activity. *Nano Energy* **51**, 26–36 (2018).
13. Huang, J. et al. Identification of key reversible intermediates in self-reconstructed nickel-based hybrid electrocatalysts for oxygen evolution. *Angew. Chem. Int. Ed.* **58**, 17458–17464 (2019).
14. Wang, J. Controlling dynamic reconstruction chemistry for superior oxygen-evolving catalysts. *Chem* **9**, 1645–1657 (2023).
15. Klápště, B., Micka, K., Mrha, J. & Vondrák, J. The nature of the second discharge step of nickel oxide electrodes. *J. Power Sources* **8**, 351–357 (1982).
16. Dionigi, F. et al. In-situ structure and catalytic mechanism of NiFe and CoFe layered double hydroxides during oxygen evolution. *Nat. Commun.* **11**, 2522 (2020).
17. Li, Y.-F., Li, J.-L. & Liu, Z.-P. Structure and catalysis of NiOOH: recent advances on atomic simulation. *J. Phys. Chem. C* **125**, 27033–27045 (2021).
18. Friebel, D. et al. Identification of highly active fe sites in (Ni, Fe) OOH for electrocatalytic water splitting. *J. Am. Chem. Soc.* **137**, 1305–1313 (2015).
19. Yang, C. et al. Phosphate ion functionalization of perovskite surfaces for enhanced oxygen evolution reaction. *J. Phys. Chem. Lett.* **8**, 3466–3472 (2017).
20. Dhaka, K. & Exner, K. S. Degree of span control to determine the impact of different mechanisms and limiting steps: oxygen evolution reaction over Co_3O_4(001) as a case study. *J. Catal.* **443**, 115970 (2025).
21. Lang, C. et al. Observation of a potential-dependent switch of water-oxidation mechanism on Co-oxide-based catalysts. *Chem* **7**, 2101–2117 (2021).
22. Ullman, A. M., Brodsky, C. N., Li, N., Zheng, S.-L. & Nocera, D. G. Probing edge site reactivity of oxidic cobalt water oxidation catalysts. *J. Am. Chem. Soc.* **138**, 4229–4236 (2016).
23. Li, L.-F., Li, Y.-F. & Liu, Z.-P. Oxygen evolution activity on NiOOH catalysts: four-coordinated Ni cation as the active site and the hydroperoxide mechanism. *ACS Catal.* **10**, 2581–2590 (2020).
24. Zhang, M., de Respinis, M. & Frei, H. Time-resolved observations of water oxidation intermediates on a cobalt oxide nanoparticle catalyst. *Nat. Chem.* **6**, 362–367 (2014).
25. Zhang, N. et al. Lattice oxygen activation enabled by high-valence metal sites for enhanced water oxidation. *Nat. Commun.* **11**, 4066 (2020).
26. Wang, X. et al. Pivotal role of reversible NiO_6 geometric conversion in oxygen evolution. *Nature* **611**, 702–708 (2022).
27. Lee, S., Chu, Y. C., Bai, L., Chen, H.-M. & Hu, X. Operando identification of a side-on nickel superoxide intermediate and the mechanism of oxygen evolution on nickel oxyhydroxide. *Chem Catal.* **3**, 100475 (2023).
28. Lee, H.-S. et al. Electrochemically generated electrophilic peroxo species accelerates alkaline oxygen evolution reaction. *Joule* **7**, 1902–1919 (2023).
29. Rao, R. R. et al. Spectroelectrochemical analysis of the water oxidation mechanism on doped nickel oxides. *J. Am. Chem. Soc.* **144**, 7622–7633 (2022).
30. Xu, S. et al. Dual-site segmentally synergistic catalysis mechanism: boosting $CoFeS_x$ nanocluster for sustainable water oxidation. *Nat. Commun.* **15**, 1720 (2024).
31. Hao, Y. et al. Recognition of surface oxygen intermediates on NiFe oxyhydroxide oxygen-evolving catalysts by homogeneous oxidation reactivity. *J. Am. Chem. Soc.* **143**, 1493–1502 (2021).
32. Kang, J. et al. Realizing two-electron transfer in $Ni(OH)_2$ nanosheets for energy storage. *J. Am. Chem. Soc.* **144**, 8969–8976 (2022).
33. Ferreira de Araújo, J., Dionigi, F., Merzdorf, T., Oh, H. S. & Strasser, P. Evidence of Mars–van-Krevelen mechanism in the electrochemical oxygen evolution on Ni-based catalysts. *Angew. Chem. Int. Ed.* **60**, 14981–14988 (2021).
34. Cheng, W. et al. Lattice-strained metal–organic-framework arrays for bifunctional oxygen electrocatalysis. *Nat. Energy* **4**, 115–122 (2019).
35. Görlin, M. et al. Tracking catalyst redox states and reaction dynamics in Ni–Fe oxyhydroxide oxygen evolution reaction electrocatalysts: the role of catalyst support and electrolyte pH. *J. Am. Chem. Soc.* **139**, 2070–2082 (2017).
36. Ding, Y., Du, J., Wang, T. & Sun, L. Identifying the active site of water oxidation catalyst based on defective Fe-doped Ni oxyhydroxide. *CCS Chem.* **6**, 365–376 (2024).
37. Wang, Z., Goddard, W. A. & Xiao, H. Potential-dependent transition of reaction mechanisms for oxygen evolution on layered double hydroxides. *Nat. Commun.* **14**, 4288 (2023).
38. Dickens, C.-F., Kirk, C. & Nørskov, J. K. Insights into the electrochemical oxygen evolution reaction with ab initio calculations and microkinetic modeling: beyond the limiting potential volcano. *J. Phys. Chem. C* **123**, 18960–18977 (2019).
39. Velasco-Velez, J.-J. et al. The structure of interfacial water on gold electrodes studied by X-ray absorption spectroscopy. *Science* **346**, 831–834 (2014).
40. Farmand, M. et al. Electrochemical flow cell enabling operando probing of electrocatalyst surfaces by X-ray spectroscopy and diffraction. *Phys. Chem. Chem. Phys.* **21**, 5402–5408 (2019).
41. Prajapati, A. et al. Best practices for in-situ and operando techniques within electrocatalytic systems. *Nat. Commun.* **16**, 2593 (2025).
42. Deng, B. et al. A self-circulating pathway for the oxygen evolution reaction. *Energy Environ. Sci.* **16**, 5210–5219 (2023).
43. Wei, J. et al. Sequential oxygen evolution and decoupled water splitting via electrochemical redox reaction of nickel hydroxides. *Nat. Commun.* **15**, 9012 (2024).

44. Dotan, H. et al. Decoupled hydrogen and oxygen evolution by a two-step electrochemical–chemical cycle for efficient overall water splitting. *Nat. Energy* **4**, 786–795 (2019).
45. Smith, R. D. L. & Berlinguette, C. P. Accounting for the dynamic oxidative behavior of nickel anodes. *J. Am. Chem. Soc.* **138**, 1561–1567 (2016).
46. Yao, N. et al. Atomically dispersed Ru oxide catalyst with lattice oxygen participation for efficient acidic water oxidation. *Chem* **9**, 1882–1896 (2023).
47. Huang, Z.-F. et al. Chemical and structural origin of lattice oxygen oxidation in Co–Zn oxyhydroxide oxygen evolution electrocatalysts. *Nat. Energy* **4**, 329–338 (2019).
48. Qin, R. et al. Achieving high stability and rate performance using spherical nickel–zinc layered double hydroxide in alkaline solution. *J. Electrochem. Soc.* **168**, 070539 (2021).
49. Trześniewski, B. J. et al. In situ observation of active oxygen species in Fe-containing Ni-based oxygen evolution catalysts: the effect of pH on electrochemical activity. *J. Am. Chem. Soc.* **137**, 15112–15121 (2015).
50. Lee, S., Banjac, K., Lingenfelder, M. & Hu, X. Oxygen isotope labeling experiments reveal different reaction sites for the oxygen evolution reaction on nickel and nickel iron oxides. *Angew. Chem. Int. Ed.* **58**, 10295–10299 (2019).
51. Hao, Y. et al. Chemical oxygen species on electrocatalytic materials during oxygen evolution reaction. *Mater. Today Catal.* **2**, 100012 (2023).
52. Hu, C. et al. Surface-enhanced raman spectroscopic evidence of key intermediate species and role of NiFe dual-catalytic center in water oxidation. *Angew. Chem. Int. Ed.* **60**, 19774–19778 (2021).
53. Yang, Y. et al. The identity of nickel peroxide as a nickel superoxyhydroxide for enhanced electrocatalysis. *JACS Au* **3**, 2964–2972 (2023).

Methods

A-NiOOH preparation

To obtain more A-NiOOH, a standard three-electrode configuration was used for the galvanostatic electrolysis process. NiOOH on nickel foam (NiOOH/NF; effective geometric surface area, 1 cm × 1 cm) was used as the working electrode, a graphite rod was used as the counter-electrode and a Hg/HgO electrode was used as the reference electrode. After galvanostatic electrolysis at 500 mA cm^{-2} for 5 min in 1.0 M KOH, A-NiOOH was formed on the NiOOH/NF. The sample was quickly rinsed with deionized water and then treated in liquid nitrogen for further processing in a freeze-dryer for 12 h to remove water, resulting in A-NiOOH/NF. Black powder A-NiOOH was peeled off from the surface of NF for further characterization and activity testing. A-NiOOH remains active after a few days in the air and can be stored in a glovebox for several months. It is important to note that the required NiOOH is not limited to this synthetic method. This method was chosen because it can achieve a high loading of NiOOH, thus providing sufficient A-NiOOH for subsequent experiments.

Clark-type oxygen electrode measurements

We tested the oxygen release concentration of all samples in deoxygenated aqueous solutions using an Oxygraph+ Clark-type liquid electrode (Hansatech Oxytherm, Hansatech Instruments). Initially, the water solution was continuously purged with nitrogen gas, and the oxygen electrode signal was set to zero once it stabilized at an extremely low level, establishing the zero-oxygen baseline. Subsequently, the oxygen electrode signal measured in O_2-saturated water was used to set the oxygen saturation line. During the sample addition process, nitrogen gas is continuously supplied to prevent air from dissolving into the aqueous solution. Finally, the sample inlet is sealed with a stopper, and the changes in oxygen concentration within the sealed chamber are monitored. Additionally, we measured the oxygen release from anhydrous solid samples under the same nitrogen-purging conditions using an optical oxygen sensor (OceanInsight) and set the zero-oxygen baseline. The oxygen content in air was also used as a calibration value.

OLMS measurements

All gas identification experiments (including in acid $H_2{}^{18}O$) were conducted using an OLMS system provided by Linglu Instruments (Shanghai). To make our experimental operations more suitable, we made improvements to the OLMS reaction vessel. We used a sealed container with an adapted inlet hole and a tightly coverable PTFE membrane. Specifically, we first remove the dissolved oxygen in the solution by purging with nitrogen and confirm that the real-time OLMS signal meets the baseline requirements. Then, while adding the sample, we continuously flow nitrogen to purge the inlet. Finally, we quickly add the sample and tighten the rubber stopper to obtain the real-time signal changes.

Computational models and methods

All the spin-polarized DFT calculations in the work were carried out using the Vienna Ab initio Simulation Package[54,55] by the projector-augmented wave pseudopotential method[55,56]. All electronic structures were calculated using the generalized gradient approximation with Perdew–Burke–Ernzerhof[57] expansion on the plane-wave basis[54,58] with a cut-off energy set to 400 eV. Hubbard-*U* correction was included to account for the strong correlation in the 3*d* orbitals, with the *U*–*J* terms of nickel being 5.2 eV (ref. 16).

Although the active phase of NiOOH has been identified as the γ-phase, the low crystallinity and high structural complexity of this phase make it difficult to construct a rational structure. However, the β-phase NiOOH offers a well-defined alternative structure. Therefore, the active γ-phase NiOOH can be formed by removing partial interlaminar protons from the β-phase NiOOH bulk, resulting in an average oxidation state of +3.75 to match the experiment[37]. Then, *p*(4 × 1) NiOOH (100) facets were modelled with four layers, in which the bottom two layers were fixed, while the other layers were fully relaxed. An ~15-Å vacuum layer was used to eliminate the interaction between neighbouring slabs. A 2 × 4 × 1 Monkhorst–Pack *k*-point mesh sampling for Brillouin-zone integration was used to optimize all surface structures.

Both explicit and implicit solvation effects were taken into account. The van der Waals interaction was described by the DFT-D3 method[59,60]. The equilibrium was achieved when the forces on the relaxed atoms and the energies in the self-consistent iterations became less than 0.05 eV $Å^{-1}$ and 10^{-5} eV, respectively. The computational hydrogen electrode method[61,62] was used to describe the free energies of the proton–electron pair in the electrocatalytic process. Transition states were located using the climbing-image nudged elastic band method[63,64]. All structures are ferromagnetic.

Role of the Ni–O–O–Ni_2 structure

The presence of the embedded Ni–O–O–Ni_2 species has three crucial roles in the overall surface reactions. First, it maintains the high-valence state of the surrounding nickel ions, which serve as potential active sites for water oxidation. Second, it facilitates the O–O coupling process, as evidenced by the lower reaction free energy near the Ni–O–O–Ni_2 structure compared with regions distant from it (Supplementary Fig. 28), the processes of which are barrierless. Third, it reduces the activation barrier for the continuous proton-transfer process, with the first hydrogen-transfer step near the Ni–O–O–Ni_2 structure requiring only 1.18 eV compared with 1.50 eV far from it (Supplementary Fig. 29), thereby promoting proton transfer from the surface into the bulk.

Data availability

All data involved in this study are available in the main text and the Supplementary Information files. The raw data for the figures in this paper are provided in the Source Data and are publicly available. Source data are provided with this paper.

References

54. Kresse, G. & Furthmüller, J. Efficient iterative schemes for ab initio total-energy calculations using a plane-wave basis set. *Phys. Rev. B* **54**, 11169–11186 (1996).
55. Kresse, G. & Joubert, D. From ultrasoft pseudopotentials to the projector augmented-wave method. *Phys. Rev. B* **59**, 1758–1775 (1999).
56. Blöchl, P. E. Projector augmented-wave method. *Phys. Rev. B* **50**, 17953–17979 (1994).
57. Perdew, J. P., Burke, K. & Ernzerhof, M. Generalized gradient approximation made simple. *Phys. Rev. Lett.* **77**, 3865–3868 (1996).
58. Kresse, G. & Furthmüller, J. Efficiency of ab-initio total energy calculations for metals and semiconductors using a plane-wave basis set. *Comput. Mater. Sci.* **6**, 15–50 (1996).
59. Grimme, S., Antony, J., Ehrlich, S. & Krieg, H. A consistent and accurate ab initio parametrization of density functional dispersion correction (DFT-D) for the 94 elements H–Pu. *J. Chem. Phys.* **132**, 154104 (2010).
60. Grimme, S., Ehrlich, S. & Goerigk, L. Effect of the damping function in dispersion corrected density functional theory. *J. Comput. Chem.* **32**, 1456–1465 (2011).
61. Nørskov, J. K. et al. Origin of the overpotential for oxygen reduction at a fuel-cell cathode. *J. Phys. Chem. B* **108**, 17886–17892 (2004).
62. Peterson, A. A., Abild-Pedersen, F., Studt, F., Rossmeisl, J. & Nørskov, J. K. How copper catalyzes the electroreduction of carbon dioxide into hydrocarbon fuels. *Energy Environ. Sci.* **3**, 1311–1315 (2010).
63. Henkelman, G. & Jónsson, H. Improved tangent estimate in the nudged elastic band method for finding minimum energy paths and saddle points. *J. Chem. Phys.* **113**, 9978–9985 (2000).

64. Henkelman, G., Uberuaga, B. P. & Jónsson, H. A climbing image nudged elastic band method for finding saddle points and minimum energy paths. *J. Chem. Phys.* **113**, 9901–9904 (2000).

Acknowledgements

This work is financially supported by the National Key R&D Program of China (2022YFC3401800 to B.Z.), the National Natural Science Foundation of China (22279105 to B.Z.), the Zhejiang Provincial Natural Science Foundation (XHD24B0201 to B.Z.), a start-up package from Westlake University, the Kunpeng Research Fund from Zhejiang Province, the Research Center for Industries of the Future and Zhejiang Baima Lake Laboratory. We thank T. Wang for discussions about the DFT calculations. We thank the Center of Artificial Photosynthesis (CAP) for Solar Fuels at Westlake University for academic and instrument support. We thank the Instrumentation and Service Center for Physical Sciences (ISCPS) and the Instrumentation and Service Center for Molecular Sciences (ISCMS) at Westlake University for the facility support and technical assistance. We thank the Westlake University HPC Center for computation support.

Author contributions

L.S. and B.Z. supervised this project. X. Cui designed and conducted the experiments, data analysis of electrochemical experiments, crystallography, spectroscopic experiments, and wrote the paper. Y.D. carried out DFT calculations and wrote this part of the paper. F.Z. and X. Cao analysed and discussed the results. Y.G. discussed the DFT calculations. L.S. and B.Z. revised and edited the manuscript, and were responsible for funding acquisition and project administration. All authors participated in discussions and manuscript proofreading.

Competing interests

The authors declare no conflict of interest.

Additional information

Supplementary information The online version contains supplementary material available at https://doi.org/10.1038/s41557-025-01942-5.

Correspondence and requests for materials should be addressed to Biaobiao Zhang.

Peer review information *Nature Chemistry* thanks Kai S. Exner and the other, anonymous, reviewer(s) for their contribution to the peer review of this work.